ADVANCED FUNCTIONAL MATERIALS
www.afm-journal.de

Catalyst-Free Growth of Atomically Thin Bi_2O_2Se Nanoribbons for High-Performance Electronics and Optoelectronics

Usman Khan, Lei Tang, Baofu Ding, Luo Yuting, Simin Feng, Wenjun Chen, Muhammad Jahangir Khan, Bilu Liu, and Hui-Ming Cheng**

1D materials have attracted significant research interest due to their unique quantum confinement effects and edge-related properties. Atomically thin 1D nanoribbons are particularly interesting because it is a valuable platform with the physical limits of both thickness and width. Here, a catalyst-free growth method is developed and the growth of Bi_2O_2Se nanostructures with tunable dimensionality is achieved. Significantly, Bi_2O_2Se nanoribbons with a thickness down to 0.65 nm, corresponding to a monolayer, are successfully grown for the first time. Electrical and optoelectronic measurements show that Bi_2O_2Se nanoribbons possess decent performance in terms of mobility, on/off ratio, and photoresponsivity, suggesting their promise for devices. This work not only reports a new method for the growth of atomically thin nanoribbons but also provides a platform to study properties and applications of such nanoribbon materials at a thickness limit.

1. Introduction

Dimensionality engineering of materials has been an effective strategy to manipulate their electronic, optical, magnetic, and catalytic properties.[1] 1D structure is important because of its unique properties including edge states,[2] quantum confinement,[3] ferromagnetic feature,[4] and high integration density for devices.[5] In the past two decades, researchers have shown extensive interests to study 1D materials like nanoribbon, nanotube, nanowire, and nanobelt. Recently, there is a trend to prepare 1D nanoribbons from monolayer 2D materials to make atomically thin nanoribbons and to explore their properties at physical limits of both thickness and width. For example, graphene nanoribbon possesses sizeable bandgaps which are sensitive to its width, expanding the use of graphene in digital electronics. Regarding 2D transition metal dichalcogenides, researchers have shown that MoS_2 nanoribbon is more stable than MoS_2 nanocluster and can exhibit intrinsic magnetism under certain edge structures without the introduction of metal doping in nonmagnetic MoS_2.[2a] In another material example, it is reported that black phosphorus nanoribbons have a different effective mass of charged carriers and bandgaps, making them promising for optoelectronics and valleytronics.[6] It is clear that modulating the properties of materials is important and dimensionality engineering is an effective strategy.

Among 2D materials, Bi_2O_2Se has been synthesized only recently with exotic properties and emerged as a promising candidate for future electronics and optoelectronics.[7] The 2D Bi_2O_2Se has been incorporated in applications including field-effect transistors (FETs),[8] infrared photodetection,[9] spintronics,[10] photothermal therapy, and photoacoustic applications.[11] Similar to other 2D materials, the growth of atomically thin Bi_2O_2Se nanoribbons is highly motivated. However, there is very rare research in growing Bi_2O_2Se nanoribbons. Recently, Tan et. al. developed a bismuth-catalyzed vapor–liquid–solid (VLS) mechanism to grow Bi_2O_2Se nanoribbons and studied their use in FET.[12] The thickness of the thinnest VLS grown nanoribbon was around 5 nm, corresponding to 8 atomic layers. FETs based on these Bi_2O_2Se nanoribbons revealed a decent current on/off ratio of $>10^6$ and a room temperature field-effect mobility of 220 $cm^2\ v^{-1}\ s^{-1}$. It is intriguing to explore the growth and properties of monolayer Bi_2O_2Se nanoribbons, which is not reported previously. In addition, catalysts might raise impurities to Bi_2O_2Se nanoribbons during the VLS growth process. The metal contamination may introduce energy levels in the bandgap of semiconductors and, influence their optical and electrical performance.[13] Therefore, the development of catalyst-free growth method and exploiting properties of Bi_2O_2Se nanoribbons down to one monolayer are essential but remain challenging.

Here, we developed a catalyst-free chemical vapor deposition (CVD) method for the synthesis of Bi_2O_2Se nanostructures with

Dr. U. Khan, L. Tang, Dr. B. Ding, Dr. L. Yuting, Dr. S. Feng, Dr. W. Chen, M. J. Khan, Prof. B. Liu, Prof. H.-M. Cheng
Shenzhen Geim Graphene Center
Tsinghua-Berkeley Shenzhen Institute & Institute of Materials Research
Tsinghua Shenzhen International Graduate School
Tsinghua University
Shenzhen 518055, P. R. China
E-mail: bilu.liu@sz.tsinghua.edu.cn; hmcheng@sz.tsinghua.edu.cn
Prof. H.-M. Cheng
Shenyang National Laboratory for Materials Science
Institute of Metal Research
Chinese Academy of Sciences
Shenyang 110016, P. R. China
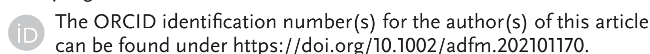
The ORCID identification number(s) for the author(s) of this article can be found under https://doi.org/10.1002/adfm.202101170.

DOI: 10.1002/adfm.202101170

 © 2021 Wiley-VCH GmbH

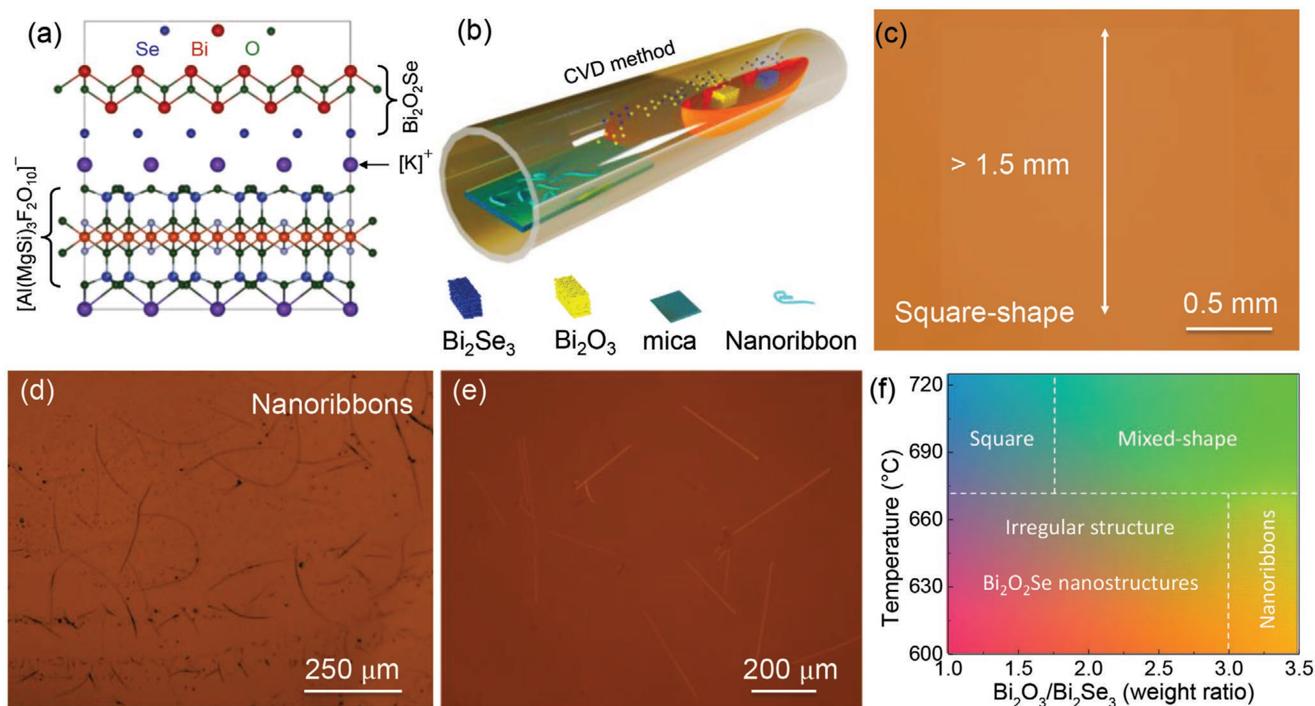

Figure 1. Catalyst-free CVD for the growth of Bi_2O_2Se nanostructures with tunable dimensionality. a) Schematic illustration of the planar growth of Bi_2O_2Se on mica. b) Schematic illustration for CVD growth of Bi_2O_2Se nanostructures with tunable morphology such as 2D quadrilateral Bi_2O_2Se and 1D Bi_2O_2Se nanoribbons whereas dual precursors of Bi_2O_3 and Bi_2Se_3 are used in CVD growth. c) A typical OM image of square-shaped Bi_2O_2Se with an average domain size of >1.5 mm. OM images of Bi_2O_2Se nanoribbons of d) low resolution and e) high-resolution image. f) The schematic design of the morphology control of Bi_2O_2Se nanostructures via tuning temperature and the weight ratio of Bi_2O_3 and Bi_2Se_3 precursors.

tunable dimensionality. By controlling the precursor ratio of Bi_2O_3 and Bi_2Se_3 in the furnace, the growth of 2D Bi_2O_2Se quadrilaterals can be precisely controlled and consequently Bi_2O_2Se nanoribbons with thickness down to monolayer are grown. The CVD grown Bi_2O_2Se nanoribbon-based FET exhibited a high current on/off ratio of $>10^7$, and high electron mobility of ≈262 $cm^2\ V^{-1}\ s^{-1}$. Moreover, photodetectors of Bi_2O_2Se nanoribbons show a high photoresponsivity of $\approx 9.2 \times 10^6$ A W^{-1}. The successful growth of Bi_2O_2Se nanoribbons with atomically thin thickness and decent device performance suggest its great potential for electronic and optoelectronic applications.

2. Results and Discussion

Bi_2O_2Se nanostructures are grown by CVD on a mica ($KMg_3AlSi_3O_{10}F_2$) substrate. The growth of Bi_2O_2Se nanostructures on mica is based on electrostatic interaction between K^+ layer of mica and Se^{2-} layer of Bi_2O_2Se as shown in **Figure 1**a. Combining the electrostatic interaction between mica and Bi_2O_2Se facilitates the lateral growth of nanostructures. The atomically thin growth of 2D Bi_2O_2Se results because of the lower energy barrier. Dual precursors Bi_2O_3 and Bi_2Se_3 were utilized as co-evaporation sources for the CVD growth of Bi_2O_2Se. The experimental setup for the growth of Bi_2O_2Se nanostructures is illustrated in Figure 1b. The typical square-shaped optical microscope (OM) image of Bi_2O_2Se is shown in Figure 1c. The 2D Bi_2O_2Se nanoplate has an ultrasmooth large single crystal with domain size in the range of millimeters. Notably, Bi_2O_2Se with a large domain size of ≈1.5 mm were obtained by precisely controlling the growth parameters including growth time, growth temperature, and gas flow rate. It was observed that the growth temperature and weight ratio of precursors had a strong impact on the morphology of Bi_2O_2Se. Therefore, more precise experiments were conducted by tuning the growth temperature concerning the weight ratio of precursor powders to achieve atomically thin Bi_2O_2Se nanostructures. It was predicted that the synthesis of Bi_2O_2Se nanoribbon went through different growth stages and details are given in Supporting Information. As for the growth mechanism of Bi_2O_2Se nanoribbon, we consider that the cap-mediated vapor–solid–solid (VSS) growth mode contributes to the growth results. During the growth process, the powder of precursors (Bi_2O_3 and Bi_2Se_3) is first heated to grow the Bi_2O_2Se cap. Then, with the constant feeding of vapor precursors, the initial Bi_2O_2Se cap will continue to incorporate precursors through the vapor/solid interface, ultimately resulting in the supersaturation of Bi_2O_2Se. Finally, the further addition of the precursors into the Bi_2O_2Se cap will eventually result in the precipitates, which creates a solid/solid interface as the growth interface (Figure S1, Supporting Information). It is important to mention that this is a first report on the growth of monolayer Bi_2O_2Se nanoribbons despites its importance for the fundamental understanding of the layer-dependent growth mechanism of this material. The successful growth of monolayer Bi_2O_2Se nanoribbons provides a material platform to study the physical

 © 2021 Wiley-VCH GmbH

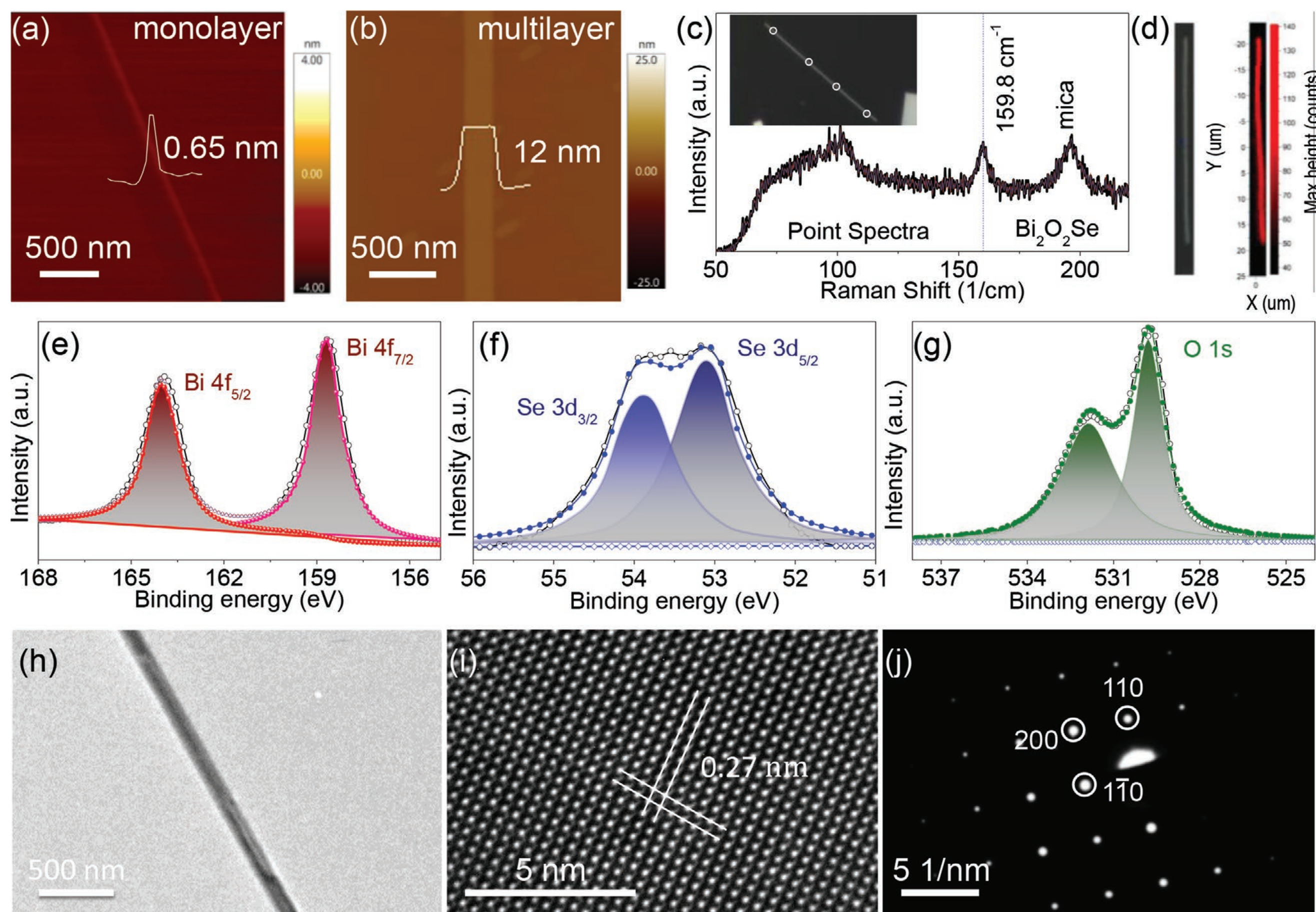

Figure 2. Characterization of monolayer and few-layer Bi_2O_2Se nanoribbons. a) AFM image of a monolayer Bi_2O_2Se nanoribbon with a thickness of ≈0.65 nm and a width of ≈80 nm. b) AFM image of a multilayer Bi_2O_2Se nanoribbon with a thickness of ≈12 nm. c) Point spectra of Bi_2O_2Se nanoribbon collected at different points indicating by white circles in the inset. d) Raman mapping of the nanoribbon recorded at A_{1g} vibrational mode. e–g) XPS spectra of the few-layer Bi_2O_2Se nanoribbons. h) TEM image of Bi_2O_2Se nanoribbon. i) HRTEM image of nanoribbon indicating lattice spacing of 0.27 nm for (110) plane. j) A SAED pattern of Bi_2O_2Se nanoribbon representing its single crystalline feature.

properties of such materials at thickness limit, for example, edge states, quantum confinement, and ferromagnetic feature. As shown in Figure 1d, the as-grown flakes have nanoribbon-like-morphology with an average width and length ≈80 nm and ≈200 µm, respectively. The high-magnification OM image of Bi_2O_2Se nanoribbons is shown in Figure 1e. It has been observed that the weight ratio of precursors and growth temperature play important roles in achieving nanostructures with multi-dimensionality including square-shaped Bi_2O_2Se, rectangular-shaped-Bi_2O_2Se, and ribbon-like morphology of Bi_2O_2Se as summarized in Figure 1f. It is worth mentioning that the nanoribbons were prepared without the use of any catalysts.

Next, we focus on the topography and crystal structure of Bi_2O_2Se nanoribbons. The typical atomic force microscopy (AFM) image of Bi_2O_2Se nanoribbon is displayed in **Figure 2**a and shows that the topography of the nanoribbon is clean and homogeneous. The thickness of the sample is ≈0.65 nm corresponds to the thickness of the monolayer with a width of ≈80 nm. Multilayer Bi_2O_2Se nanoribbons have also been synthesized by the CVD method, one sample of which has a thickness of ≈12 nm as shown in Figure 2b. Furthermore, Raman spectroscopy of CVD grown multilayer Bi_2O_2Se nanoribbon is conducted at white circular areas highlighted in the inset of Figure 2c. The point spectra at various positions have analogous characteristic A_{1g} peaks which are centered at ≈159 cm^{-1}. In addition, Raman mapping of the characteristic peak A_{1g} of nanoribbon depicts similar color contrast across the whole region, indicating the homogeneity of the sample as shown in Figure 2d. Next, we examined the quality of CVD grown samples based on the chemical composition and crystal structure of Bi_2O_2Se nanoribbons. X-ray photoelectron spectroscopy (XPS) confirms the chemical bonding states of Bi, Se, and O as shown in Figure 2e–g. The quantitative investigation indicates Bi to Se atomic ratio of 2:1, demonstrating the formation of nanoribbons with adequate stoichiometry. The XPS spectrum of Bi is fitted with two peaks, centered at ≈164 and ≈159 eV which are corresponding peaks of metallic Bi in bismuth oxide. The fitted peaks of Se $3d_{3/2}$ and Se $3d_{5/2}$ are centered at 54 and 53.1 eV. All the identified peaks have their binding energies consistent with the composition of Bi_2O_2Se nanoribbons. This attributes that the excess amount of Bi_2O_3 in synthesized Bi_2O_2Se nanoribbons samples does not affect the elemental composition and

© 2021 Wiley-VCH GmbH

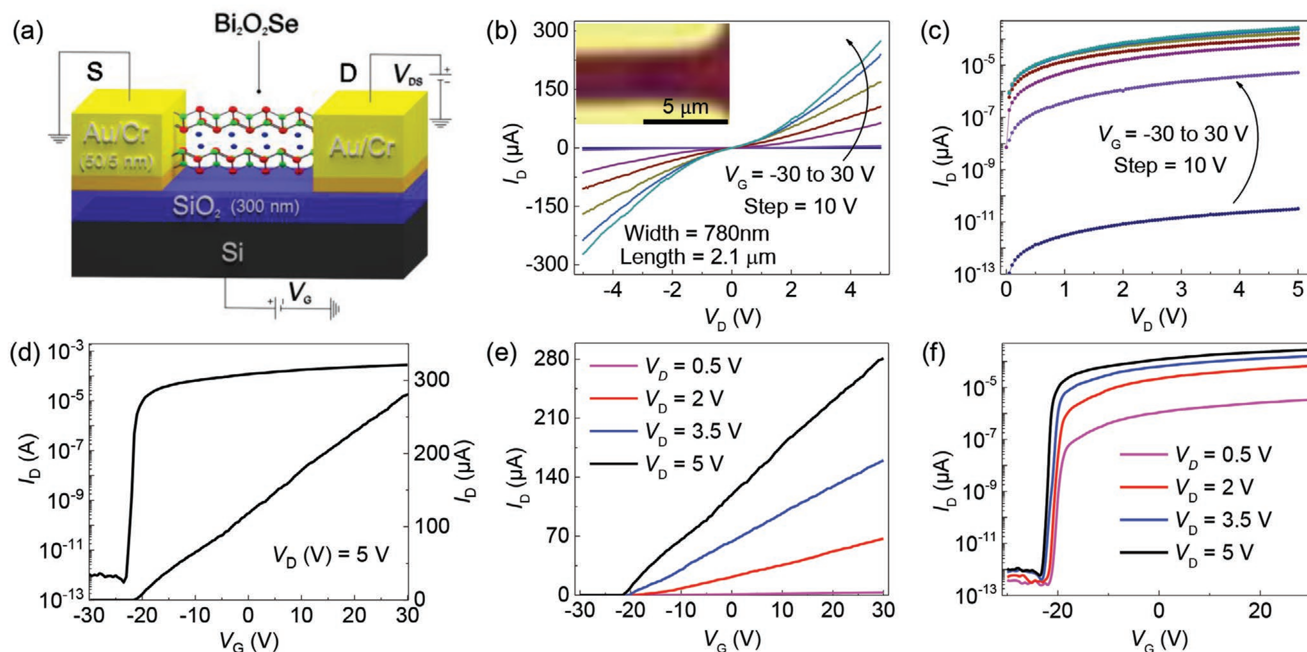

Figure 3. Electrical performance of 1D Bi_2O_2Se nanoribbon. a) Schematic illustration of back-gated Bi_2O_2Se nanoribbon-based FET. b) The inset depicts OM of Bi_2O_2Se nanoribbon-based FET device with a channel length (L) and width (W) of 2.1 µm and 780 nm, respectively, whereas the main figure indicates output characteristic curves (I_D–V_D) of the device as a function of gate voltage (V_G) in linear scale (b) and logarithmic scale (c). d) The transfer characteristic curves (I_D–V_G) at V_D of 5 V. e,f) I_D–V_G family curves of the device as a function of V_D are represented in linear and logarithmic scales.

reveals consistency with the published work.[14] Transmission electron microscope (TEM) was employed to further investigate the lattice parameter and crystal structure of Bi_2O_2Se nanoribbons. Figure 2h depicts a typically transferred nanoribbon on Cu grid without any damage. A high-resolution TEM (HRTEM) image of Bi_2O_2Se nanoribbon indicates a d-spacing of 2.7 Å which is accordant with (110) plane of Bi_2O_2Se (Figure 2i).[14,15] The single crystal behavior of the nanoribbon was further analyzed by a selected area electron diffraction (SAED) image that confirms high crystal quality. The bright spots in the pattern (200), $(1\bar{1}0)$, and (110) indicate the tetragonal structure of nanoribbon as shown in Figure 2j. Overall, the analyses indicate that CVD-grown Bi_2O_2Se nanoribbon has good uniformity, stoichiometry, and high quality.

Previous studies have shown that atomically thin 2D Bi_2O_2Se nanoflakes represent a high electronic response which further motivates the fabrication of FET based on Bi_2O_2Se nanoribbons. Therefore, considering the importance of Bi_2O_2Se nanoribbons for electronic and optoelectronic applications, samples were initially transferred on an SiO_2/Si substrate. To investigate the electrical performance of Bi_2O_2Se nanoribbons, the transport measurements were investigated with a back-gated FET configuration to determine the feature of thick nanoribbon (12 nm) and studied the contact behavior among nanoribbon and electrodes. The schematic illustration of Bi_2O_2Se nanoribbon-based FET is shown in **Figure 3**a. The OM image of nanoribbon-based Bi_2O_2Se FET with channel width (W) of ≈780 nm and length (L) of ≈2.1 µm is shown in the inset of Figure 3b. Output characteristic curves (I_D–V_D) of the device measured at room temperature are represented in Figure 3b. The back-gate voltage (V_G) has been tuned from -30 to 30 V with a step voltage of 10 V. It can be observed that drain current (I_D) is highly dependent on V_G which suggests desired gate controllability of the device. The non-linear nature of I_D–V_D curves describes the existence of Schottky junction with a slight difference in barrier height among Bi_2O_2Se nanoribbon and metallic electrodes at both ends of the nanoribbon. The I_D–V_D curves of nanoribbon FET show n-type semiconducting behavior in which I_D increases (decreases) with a raise in positive (negative) V_G. The current ratio amongst V_G of −30 and 30 V is ≈10^7, which is depicted from the semi-log scale drawn in Figure 3c. The room temperature transfer characteristic curves (I_D–V_G) at different V_D are shown in Figure 3d. The I_D–V_G curves delve the increase in I_D with V_G which further approves n-type conductivity of nanoribbons. The calculated field-effect carrier mobility is ≈262 $cm^2V^{-1}s^{-1}$ and the corresponding carrier density of a Bi_2O_2Se nanoribbon FET is 3.2×10^{-12} cm^{-2} at which $V_D = 5$ V. The threshold voltage is determined to be about −21 V by extrapolation of I_D–V_G curves in the linear region. Figure 3e depicts I_D–V_G curves in linear scale at different V_D representing the n-type feature of FET device. The feature is more prominent in the logarithmic scale of I_D–V_G curves (Figure 3f). **Table 1** benchmarks the typical research on nanoribbon designed by various synthesis techniques, materials, and electrical performance. We summarized some well-known research on nanoribbon-based FET such as n-type TMDCs, including MoS_2,[16] CdSe,[17] tri-chalcogenides TiS_3,[18] p-type graphene nanoribbon,[19] superlattices of AlGaN/GaN,[20] and a III–V compound like boron nitride.[21] The FET based on Bi_2O_2Se nanoribbons not only achieves high field-effect mobility in comparison with

© 2021 Wiley-VCH GmbH

Table 1. Performance comparison of nanoribbon field-effect transistors reported in the literature.

Materials	Method	Nature (-type)	FET architecture	On/off ratio	Mobility (cm^2 V^{-1} s^{-1})	Reference
Black phosphorus	Plasma etching	p	Top-gate	10^3	310	[22]
Graphene	Unzip MWCNTs	p	Back-gate	-	1500	[19a]
Graphene	Bottom-up approach	p	Back-gate	10^6	200	[19b]
hBN	MWBNNTs	n	-	-	58.8	[21]
AlGaN/GaN	Plasma etching	n	Top-gate	-	289	[20]
TiS_3	Heat treatment	n	Back-gate	10^4	2.6	[18]
CdSe	Thermal evaporation	n	Back-gate	10^4	9.6	[17]
MoS_2	Plasma etching	n	Back-gate	10^7	21.8	[16]
Bi_2O_2Se	VLS	n	Top-gate	10^6	220	[12]
Bi_2O_2Se	CVD	n	Back-gate	>10^7	≈262	This work

Notes. MWCNTs = multiwall carbon nanotubes; MWBNNTs = multiwall boron nitride nanotubes.

graphene nanoribbon but also simplifies the assembly complexity required for the opening of graphene bandgap. Overall, these experimental results show that Bi_2O_2Se nanoribbon has a high-quality feature and is a promising candidate for high-performance electronics.

Generally, few-layer semiconductors with suitable bandgaps are promising materials for photodetectors because of low energy loss during charge recombination, enhanced light absorption and better drain to source charge transfer.[23] Considering the advantage of the suitable bandgap of Bi_2O_2Se, we characterized the performance of a photodetector based on Bi_2O_2Se nanoribbon and it is illustrated in **Figure 4**a. Figure 4b reveals zero-gated I_D–V_D curves in dark and under light illumination. The I_D of the device on a linear scale at different power densities is represented in the inset of Figure 4b. The device exhibits dark current (I_D) of ≈100 µA at $V_D = \pm 5$ V. The maximum photocurrent ($I_{ph} = I_{light} - I_{dark}$) generated at $V_D = 5$ V ($V_G = 0$ V) is 130 µA under power density of 66.84 W m^{-2}. The photocurrent (I_{ph}) increases under illumination because of increased photogenerated charge density. The low power of laser light would possibly excite the electron–hole pairs in the nanoribbon. These pairs diffuse to the depletion region, where the built-in electric

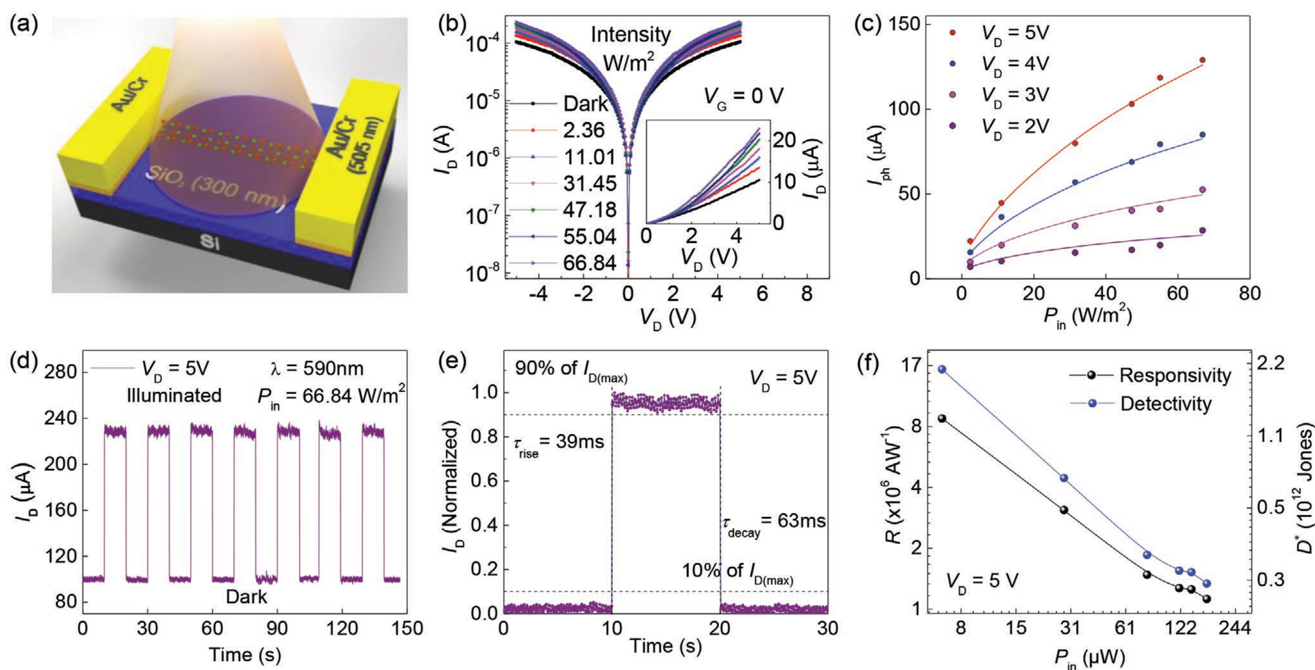

Figure 4. Optoelectronic performance of 1D Bi_2O_2Se nanoribbon. a) The output characteristic curves (I_D–V_D) of zero-gated Bi_2O_2Se nanoribbon photodetector under light illumination of 590 nm at different intensities; the linear scale of curves is shown in the inset. b) The photocurrent variation with light intensity at zero-gate bias for different drain voltages follows the power law. c) The on to off photocurrent to dark current ratio for various light intensities at zero-gate voltage. d) The on/off current switching of Bi_2O_2Se nanoribbon photodetector for laser intensity of 66.84 W m^{-2} depicts repeatability and stability of the device. e) Time-resolved photoresponse of the photodetector reveals the rise and decay times of 39 and 63 ms, respectively. f) Variation of spectral responsivity and specific detectivity of the device as a function of incident power drain voltage.

© 2021 Wiley-VCH GmbH

field is strong enough to dissociate these pairs into the free electrons and holes. The collection of these free charges by electrodes finally results in the linear increase of photocurrent. Under strong light intensity, the newly charge-balanced state stimulates incoming charge carriers at the Schottky junction and depletion region squeezes. The depletion width is consequently reduced, thereby decreasing the strength of the electric field and the resultant dissociation efficiency of electron-hole pairs. This hinders the further increase of photoresponse,[24] as presented by the saturation behavior of photocurrent ≈66.84 W m^{-2} in Figure 4b. The trend of I_{ph} as a function of different light intensities follows the power-law $I_{ph} \propto P^{\gamma}$ where γ represents I_{ph} response on light and is shown in Figure 4c. The values of the exponential function γ have been derived by a non-linear curve fitting and it yields $\gamma = 0.55$, 0.5, 0.44, and 0.39 for V_D of 5, 4, 3, and 2 V, respectively. The non-unity of γ suggests complex mechanisms that would involve charge trapping, electron-hole pair generation, and recombination in Bi_2O_2Se nanoribbons.[25] The time-resolved photoresponse of Bi_2O_2Se nanoribbon-based photodetector is measured by periodically switching of 590 nm laser light with a light intensity of 66.84 W m^{-2} at $V_D = 5$ V (Figure 4d). It can be depicted that I_D increases abruptly and becomes stabilized at ≈230 µA, followed by dropping down to the initial $I_D \approx 100$ µA after the removal of light. The device responded with an excellent on and off swapping of voltage with good stability and reproducibility which depicted the excellent reproducibility of the photodetector. The rise (τ_{rise}) and decay (τ_{decay}) time constants of the device are obtained with normalized temporal photoresponse as shown in Figure 4e. By defining τ_{rise} (τ_{decay}) as the time required by the photodetector to increase (decrease) photocurrent from 10% I_D to 90% I_D (90% I_D to 10% I_D), it is characterized to be ≈39 ms (63 ms).

The other figure of merits of the photodetectors are responsivity (R) and detectivity (D^*) and are represented in Figure 4f. The maximum spectral R of the Bi_2O_2Se photodetector has been measured to be 9.19×10^6 A W^{-1} at zero-gate voltage. The high value of R is because of a strongly induced electric field at the Bi_2O_2Se nanoribbon and metal contact Schottky junction. The corresponding value of specific detectivity at zero-gate voltage is 2.08×10^{12} Jones. The outstanding performance of the device is because of the facts: i) single-crystalline nature of nanoribbons that suppresses scattering centers and attributes more efficient carriers at contact region; and ii) absence of contamination that can deteriorate the carrier traps and reduce the non-radiative recombination centers in nanoribbons. The R as a function of light intensity is shown in Figure 4f. It is observed that the R decreases as the light intensity rises which can be elucidated as follows: three different mechanisms occur due to the irradiation of light on semiconducting nanoribbons, namely electron and hole pair generation, electron and hole pair recombination and transport of photogenerated charges due to a strong induced electric field.[25b,26] The photogenerated charge carriers are proportional to the intensity of incident light. The strongly induced field suppresses the recombination at low intensity and generates high R. Overall, these experimental results together with the tunable dimensional growth of Bi_2O_2Se depict that Bi_2O_2Se nanoribbon is a promising candidate for high-performance optoelectronics.

3. Conclusion

We have developed a catalyst-free CVD method to grow Bi_2O_2Se with tunable dimensionality ranging from 2D quadrilateral shape to 1D nanoribbons on a mica substrate. The morphology of nanostructures was controlled by tuning the growth conditions and mechanisms. Monolayer Bi_2O_2Se nanoribbons with a thickness of 0.65 nm were grown for the first time. The FETs made of Bi_2O_2Se nanoribbons exhibited n-type semiconductor characteristics with high electron mobility of ≈262 $cm^2V^{-1}s^{-1}$ and a high on/off ratio of $>10^7$. In addition, a Bi_2O_2Se nanoribbon-based photodetector exhibits a decent photoresponsivity of $\approx 9.2 \times 10^6$ A W^{-1}. Considering their high quality, good uniformity, and stoichiometry, our results suggest the potential of these monolayer thick nanoribbons for a wide range of applications.

Supporting Information

Supporting Information is available from the Wiley Online Library or from the author.

Acknowledgements

The authors acknowledge support by the National Natural Science Foundation of China (Nos. 51991340, 51920105002, 51991343, and 51950410577), Guangdong Innovative and Entrepreneurial Research Team Program (No. 2017ZT07C341), the Bureau of Industry and Information Technology of Shenzhen for the "2017 Graphene Manufacturing Innovation Center Project" (No. 201901171523), and the Shenzhen Basic Research Project (Nos. JCYJ20200109144620815, JCYJ20190809180605522, and JCYJ20200109144616617).

Conflict of Interest

The authors declare no conflict of interest.

Data Availability Statement

The data that support the findings of this study are available from the corresponding author upon reasonable request.

Keywords

Bi_2O_2Se, catalyst-free growth, chemical vapor deposition, field-effect transistor, monolayer nanoribbons, photodetectors

Received: February 3, 2021
Revised: March 23, 2021
Published online: April 28, 2021

[1] a) T. Chowdhury, J. Kim, E. C. Sadler, C. Li, S. W. Lee, K. Jo, W. Xu, D. H. Gracias, N. V. Drichko, D. Jariwala, T. H. Brintlinger, T. Mueller, H.-G. Park, T. J. Kempa, *Nat. Nanotechnol.* **2020**, *15*, 29; b) S. Li, Y.-C. Lin, W. Zhao, J. Wu, Z. Wang, Z. Hu, Y. Shen,

© 2021 Wiley-VCH GmbH

D.-M. Tang, J. Wang, Q. Zhang, H. Zhu, L. Chu, W. Zhao, C. Liu, Z. Sun, T. Taniguchi, M. Osada, W. Chen, Q.-H. Xu, A. T. S. Wee, K. Suenaga, F. Ding, G. Eda, *Nat. Mater.* **2018**, *17*, 535; c) A. Aljarb, J.-H. Fu, C.-C. Hsu, C.-P. Chuu, Y. Wan, M. Hakami, D. R. Naphade, E. Yengel, C.-J. Lee, S. Brems, T.-A. Chen, M.-Y. Li, S.-H. Bae, W.-T. Hsu, Z. Cao, R. Albaridy, S. Lopatin, W.-H. Chang, T. D. Anthopoulos, J. Kim, L.-J. Li, V. Tung, *Nat. Mater.* **2020**, *19*, 1300; d) C. Zhang, Y. Luo, J. Tan, Q. Yu, F. Yang, Z. Zhang, L. Yang, H.-M. Cheng, B. Liu, *Nat. Commun.* **2020**, *11*, 3724.

[2] a) Y. Li, Z. Zhou, S. Zhang, Z. Chen, *J. Am. Chem. Soc.* **2008**, *130*, 16739; b) H. Xu, S. Liu, Z. Ding, S. J. R. Tan, K. M. Yam, Y. Bao, C. T. Nai, M.-F. Ng, J. Lu, C. Zhang, K. P. Loh, *Nat. Commun.* **2016**, *7*, 12904.

[3] G. Liang, N. Neophytou, D. E. Nikonov, M. S. Lundstrom, *IEEE Trans. Electron Devices* **2007**, *54*, 677.

[4] G. Xu, X. Wang, Y. Sun, X. Chen, J. Zheng, L. Sun, L. Jiao, J. Li, *Nano Res.* **2015**, *8*, 2946.

[5] Z. Chen, A. Narita, K. Müllen, *Adv. Mater.* **2020**, *32*, 2001893.

[6] a) V. Tran, L. Yang, *Phys. Rev. B* **2014**, *89*, 245407; b) X. Han, H. M. Stewart, S. A. Shevlin, C. R. A. Catlow, Z. X. Guo, *Nano Lett.* **2014**, *14*, 4607; c) Z. Liu, Y. Sun, H. Cao, D. Xie, W. Li, J. Wang, A. K. Cheetham, *Nat. Commun.* **2020**, *11*, 3917; d) M. Liu, S. Feng, Y. Hou, S. Zhao, L. Tang, J. Liu, F. Wang, B. Liu, *Mater. Today* **2020**, *36*, 91.

[7] a) Q. Wei, C. Lin, Y. Li, X. Zhang, Q. Zhang, Q. Shen, Y. Cheng, W. Huang, *J. Appl. Phys.* **2018**, *124*, 055701; b) T. Cheng, C. Tan, S. Zhang, T. Tu, H. Peng, Z. Liu, *J. Phys. Chem. C* **2018**, *122*, 19970; c) M. Wu, X. C. Zeng, *Nano Lett.* **2017**, *17*, 6309; d) W. Chen, U. Khan, S. Feng, B. Ding, X. Xu, B. Liu, *Adv. Funct. Mater.* **2020**, *30*, 2004960.

[8] U. Khan, Y. Luo, L. Tang, C. Teng, J. Liu, B. Liu, H.-M. Cheng, *Adv. Funct. Mater.* **2019**, *29*, 1807979.

[9] J. Yin, Z. Tan, H. Hong, J. Wu, H. Yuan, Y. Liu, C. Chen, C. Tan, F. Yao, T. Li, Y. Chen, Z. Liu, K. Liu, H. Peng, *Nat. Commun.* **2018**, *9*, 3311.

[10] R. Quhe, J. Liu, J. Wu, J. Yang, Y. Wang, Q. Li, T. Li, Y. Guo, J. Yang, H. Peng, M. Lei, J. Lu, *Nanoscale* **2019**, *11*, 532.

[11] J. Yang, R. Quhe, Q. Li, S. Liu, L. Xu, Y. Pan, H. Zhang, X. Zhang, J. Li, J. Yan, B. Shi, H. Pang, L. Xu, Z. Zhang, J. Lu, J. Yang, *Adv. Electron. Mater.* **2019**, *5*, 1800720.

[12] C. Tan, M. Yu, S. Xu, J. Wu, S. Chen, Y. Zhao, C. Liu, Y. Zhang, T. Tu, T. Li, P. Gao, H. Peng, *Acta. Phys. Chim. Sin.* **2020**, *36*, 1908038.

[13] a) O. Moutanabbir, D. Isheim, H. Blumtritt, S. Senz, E. Pippel, D. N. Seidman, *Nature* **2013**, *496*, 78; b) J. E. Allen, E. R. Hemesath, D. E. Perea, J. L. Lensch-Falk, Z. Y. Li, F. Yin, M. H. Gass, P. Wang, A. L. Bleloch, R. E. Palmer, L. J. Lauhon, *Nat. Nanotechnol.* **2008**, *3*, 168; c) S. Francoeur, S. Tixier, E. Young, T. Tiedje, A. Mascarenhas, *Phys. Rev. B* **2008**, *77*, 085209; d) J. Zhu, H. Peng, C. K. Chan, K. Jarausch, X. F. Zhang, Y. Cui, *Nano Lett.* **2007**, *7*, 1095.

[14] J. Wu, C. Tan, Z. Tan, Y. Liu, J. Yin, W. Dang, M. Wang, H. Peng, *Nano Lett.* **2017**, *17*, 3021.

[15] J. Wu, H. Yuan, M. Meng, C. Chen, Y. Sun, Z. Chen, W. Dang, C. Tan, Y. Liu, J. Yin, Y. Zhou, S. Huang, H. Q. Xu, Y. Cui, H. Y. Hwang, Z. Liu, Y. Chen, B. Yan, H. Peng, *Nat. Nanotechnol.* **2017**, *12*, 530.

[16] H. Liu, J. Gu, P. D. Ye, *IEEE Electron Device Lett.* **2012**, *33*, 1273.

[17] J. S. Jie, W. J. Zhang, Y. Jiang, S. T. Lee, *Appl. Phys. Lett.* **2006**, *89*, 133118.

[18] J. O. Island, M. Buscema, M. Barawi, J. M. Clamagirand, J. R. Ares, C. Sánchez, I. J. Ferrer, G. A. Steele, H. S. J. van der Zant, A. Castellanos-Gomez, *Adv. Opt. Mater.* **2014**, *2*, 641.

[19] a) L. Jiao, X. Wang, G. Diankov, H. Wang, H. Dai, *Nat. Nanotechnol.* **2010**, *5*, 321; b) X. Wang, Y. Ouyang, X. Li, H. Wang, J. Guo, H. Dai, *Phys. Rev. Lett.* **2008**, *100*, 206803.

[20] S. Joglekar, M. Azize, E. J. Jones, D. Piedra, S. Gradečak, T. Palacios, *IEEE Trans. Electron Devices* **2016**, *63*, 318.

[21] H. Zeng, C. Zhi, Z. Zhang, X. Wei, X. Wang, W. Guo, Y. Bando, D. Golberg, *Nano Lett.* **2010**, *10*, 5049.

[22] X. Feng, X. Huang, L. Chen, W. C. Tan, L. Wang, K.-W. Ang, *Adv. Funct. Mater.* **2018**, *28*, 1801524.

[23] D. Lembke, S. Bertolazzi, A. Kis, *Acc. Chem. Res.* **2015**, *48*, 100.

[24] a) J. Miao, W. Hu, N. Guo, Z. Lu, X. Zou, L. Liao, S. Shi, P. Chen, Z. Fan, J. C. Ho, T.-X. Li, X. S. Chen, W. Lu, *ACS Nano* **2014**, *8*, 3628; b) Y. Hu, Y. Chang, P. Fei, R. L. Snyder, Z. L. Wang, *ACS Nano* **2010**, *4*, 1234.

[25] a) C.-H. Kuo, J.-M. Wu, S.-J. Lin, W.-C. Chang, *Nanoscale Res. Lett.* **2013**, *8*, 327; b) X. Xie, S.-Y. Kwok, Z. Lu, Y. Liu, Y. Cao, L. Luo, J. A. Zapien, I. Bello, C.-S. Lee, S.-T. Lee, W. Zhang, *Nanoscale* **2012**, *4*, 2914.

[26] a) D. Zheng, J. Wang, W. Hu, L. Liao, H. Fang, N. Guo, P. Wang, F. Gong, X. Wang, Z. Fan, X. Wu, X. Meng, X. Chen, W. Lu, *Nano Lett.* **2016**, *16*, 2548; b) E. Liu, M. Long, J. Zeng, W. Luo, Y. Wang, Y. Pan, W. Zhou, B. Wang, W. Hu, Z. Ni, Y. You, X. Zhang, S. Qin, K. W. Yi Shi, T. Taniguchi, H. Yuan, H. Y. Hwang, Y. Cui, F. Miao, D. Xing, *Adv. Funct. Mater.* **2016**, *26*, 1938.

© 2021 Wiley-VCH GmbH